Bonnet, G., et al., 2019, No large earthquakes in a fully exposed subducted seamount: Geology, https://doi.org/10.1130/G45564.1

MATERIALS AND METHODS

Thin sections of all samples were screened with the petrographic microscope. Detailed investigation of the mineralogy was carried out using the SEM facility at Institut des Sciences de la Terre de Paris (ISTeP) and Institut de Physique du Globe de Paris (IPGP).

Raman spectroscopy on carbonaceous matter (Kouketsu et al., 2014) measures the organization degree of organic matter, which irreversibly increases when heated. This method therefore provides the maximum temperature reached by a rock, with an uncertainty of ±30°C.

The (rare) presence of sodic amphibole in the massif may not in itself be characteristic of high-pressure-low-temperature metamorphism, as it is often ferric (except in pseudotachylyte).

The stability field of lawsonite in veins was modelized by a PerpleX pseudosection (Connolly, 1990, 2005) using the database of Holland and Powell (Holland et al., 1998). The bulk composition for this model is that of lawsonite, with quartz and water in excess. A similar procedure has been used to determine the stable carbonate phase (in the case of pure calcium carbonate, as attested by the chemical composition of carbonate). In every case, aragonite in thin section was only analyzed in metamorphic veins of pure calcium carbonate associated with compressional deformation. The position of other reactions in tableure 1 (albite -> jadeite + quartz; lizardite > antigorite + brucite) is from the literature (Holland, 1980; Evans, 1977).

Carbonate and serpentine polymorphs were analyzed on multiple spots in thin section (preferably on veins) using Raman spectrometry.

Thermoba-Raman-try on quartz inclusion in lawsonite (Kohn, 2014) did not give satisfactory results, most probably due to the highly non-isotropic nature of lawsonite.

The "cold subduction range" field on the P-T diagram is extracted from the compilation of shallow thermal models of subduction zones (excluding Cascadia): Costa Rica (Harris et al., 2010), Japan trench (Kimura et al., 2012), Nankai (Marcaillou et al., 2012), Makran (Smith et al., 2013).

DETAILS ON THE PSEUDOTACHYLYTE

Most of the pseudotachylyte is recrystallized, with very small (~1 µm-long) amphibole crystals.

It records different generations of crystallization/recrystallization processes:

- Very fast solidification (quench) of a melt into calcium-rich plagioclase, fassaitic clinopyroxene, glass and sulfide/oxide droplets (Fig. DR1a).
- High-pressure devitrification of the glass into rarely-preserved glaucophane (Fig. DR1b).
- Late alteration of the glass at low pressure into tremolite, albite, magnesian chlorite, quartz, albite and pumpellyite.

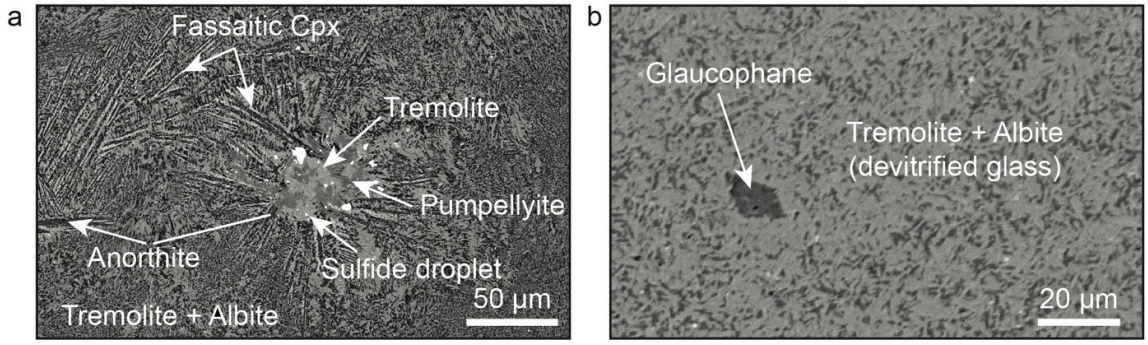

Figure DR1: SEM images of pseudotachylyte. a) Devitrified glass with radial plagioclase and high-Ti augite crystallization, and sulfide droplets; b) Glaucophane crystal in devitrified glass.

The bulk composition of the pseudotachylyte vein and the host gabbro are coherent for most elements, except for SiO_2 (pseudotachylyte) and MgO, which is possibly due to late metasomatism during the pervasive, late stage recrystallization of the pseudotachylyte at low pressure conditions.

From the dimensions of the pseudotachylyte on the field, we can estimate the seismic moment (M_0) from the following equation involving the shear modulus G, the amount of coseismic slip D, and the surface of the fault S:

$M_0 = G \times D \times S$,

which is linked to the moment magnitude by the following equation:

$M_w = \frac{2}{3} \log(M_0) - 6$.

This pseudotachylyte accommodates 1-10 cm seismic slip, and is most probably a single earthquake-related fault, given the absence of brecciation of the pseudotachylyte, the dimensions of which being on the order of 10-100 m. Therefore, we can reasonably assume a fault surface comprised between 10^2 and 10^3 m^2. By applying the shear modulus of 44 GPa determined for diabase at 0.5 GPa (Simmons and Brace, 1965), we obtain a moment magnitude between 1 and 2.4.

REFERENCES

Connolly, J.A.D., 2005, Computation of phase equilibria by linear programming: A tool for geodynamic modeling and its application to subduction zone decarbonation: Earth and Planetary Science Letters, v. 236, p. 524–541, doi: 10.1016/j.epsl.2005.04.033.

Connolly, J.A.D., 1990, Multivariable phase diagrams: an algorithm based on generalized thermodynamics: American Journal of Science, v. 290, p. 666–718, doi: 10.2475/ajs.290.6.666.

Evans, B.W., 1977, Metamorphism of Alpine Peridotite and Serpentinite: Annual Review of Earth and Planetary Sciences, v. 5, p. 397–447, doi: 10.1146/annurev.ea.05.050177.002145.

Harris, R.N., Spinelli, G., Ranero, C.R., Grevemeyer, I., Villinger, H., and Barckhausen, U., 2010, Thermal regime of the Costa Rican convergent margin: 2. Thermal models of the shallow Middle America subduction zone offshore Costa Rica: Geochemistry, Geophysics, Geosystems, v. 11, doi: 10.1029/2010GC003273.

Holland, T.J.B., 1980, The reaction albite= jadeite+ quartz determined experimentally in the range 600-1200 degrees C: American Mineralogist, v. 65, p. 129–134.

Holland, T.J.B., Baker, J., and Powell, R., 1998, Mixing properties and activity-composition relationships of chlorites in the system MgO-FeO-Al2O3-SiO2-H2O: European Journal of Mineralogy, v. 10, p. 395–406, doi: 10.1127/ejm/10/3/0395.

Kimura, G., Hina, S., Hamada, Y., Kameda, J., Tsuji, T., Kinoshita, M., and Yamaguchi, A., 2012, Runaway slip to the trench due to rupture of highly pressurized megathrust beneath the middle trench slope: The tsunamigenesis of the 2011 Tohoku earthquake off the

east coast of northern Japan: Earth and Planetary Science Letters, v. 339–340, p. 32–45, doi: 10.1016/j.epsl.2012.04.002.

Kohn, M.J., 2014, “Thermoba-Raman-try”: Calibration of spectroscopic barometers and thermometers for mineral inclusions: Earth and Planetary Science Letters, v. 388, p. 187–196, doi: 10.1016/j.epsl.2013.11.054.

Kouketsu, Y., Mizukami, T., Mori, H., Endo, S., Aoya, M., Hara, H., Nakamura, D., and Wallis, S., 2014, A new approach to develop the Raman carbonaceous material geothermometer for low-grade metamorphism using peak width: Raman CM geothermometer using FWHM: Island Arc, v. 23, p. 33–50, doi: 10.1111/iar.12057.

Marcaillou, B., Henry, P., Kinoshita, M., Kanamatsu, T., Screaton, E., Daigle, H., Harcouët-Menou, V., Lee, Y., Matsubayashi, O., Kyaw Thu, M., Kodaira, S., and Yamano, M., 2012, Seismogenic zone temperatures and heat-flow anomalies in the To-nankai margin segment based on temperature data from IODP expedition 333 and thermal model: Earth and Planetary Science Letters, v. 349–350, p. 171–185, doi: 10.1016/j.epsl.2012.06.048.

Simmons, G., and Brace, W.F., 1965, Comparison of static and dynamic measurements of compressibility of rocks: Journal of Geophysical Research, v. 70, p. 5649–5656, doi: 10.1029/JZ070i022p05649.

Smith, G.L., McNeill, L.C., Wang, K., He, J., and Henstock, T.J., 2013, Thermal structure and megathrust seismogenic potential of the Makran subduction zone: Geophysical Research Letters, v. 40, p. 1528–1533, doi: 10.1002/grl.50374.

TABLE DR1: LOCATION OF METAMORPHIC SAMPLES

Sample	Description	Unit	Latitude	Longitude	Lawsonite	Aragonite	Glaucophane
So14-28	Fracture in basalt	B	28°28'49.5"	56°52'15.6"			
So15-18	Rhyolite	A1	28°27.462'	56°50.738'	x	x	
So15-29	Lawsonite vein in andesite	B	28°30.887'	56°51.725'	x		
So15-30	Pseudotachylite and host gabbro	B	28°30.935'	56°51.572'	x		x
So15-31	Gabbro	B	28°30.963'	56°51.525'	x		
So15-32	Gabbro	B	28°31.082'	56°51.397'	x		
So16-07	Basalt	A1	28°32.719'	56°47.345'	x		
So16-09	Basalt	A2	28°32.945'	56°47.754'		x	
So16-10	Basalt	A2	28°32.099'	56°48.698'		x	
So16-25	Lawsonite vein in andesite	B	28°30.870'	56°51.719'	x		
So16-34	Basalt	A1'	28°26.821'	56°48.278'		x	
So16-37	Pillow breccia	B	28°30.045'	56°51.600'		x	
So16-40	Lawsonite vein in basalt	A2	28°30.321'	56°50.949'	x		
So17-02	Tuff	A2	28°32.924'	56°47.980'		x	
So17-04	Hydrothermal basalt	A2	28°32.225'	56°48.663'		x	
So17-14	Tuff	A1	28°28.702'	56°48.841'		x	
So17-16	Lawsonite vein in basalt	B	28°30.658'	56°50.891'	x		
So17-17	Gabbro	B	28°30.718'	56°50.878'	x		
So17-19	Basalt	A3	28°30.774'	56°50.642'		x	
So17-21	Lawsonite vein in basalt	A2	28°30.217'	56°50.895'	x		
So17-27	Gabbro	B	28°30.722'	56°51.296'	x		
So17-28	Gabbro	B	28°30.732'	56°51.308'	x		
So17-29	Basalt	B	28°30.745'	56°51.312'	x		
So17-30	Gabbro	B	28°30.752'	56°51.320'	x		
So17-31	Gabbro	B	28°30.864'	56°51.443'	x		
So17-32	Gabbro	B	28°30.852'	56°51.519'		x	
So17-33	Gabbro	B	28°30.940'	56°51.577'	x		
So17-34	Gabbro	B	28°31.128'	56°51.525'	x		
So17-35	Basalt	B	28°31.128'	56°51.525'	x		
So17-36	Lawsonite vein in basalt	B	28°31.133'	56°51.401'	x		
So17-38	Gabbro	B	28°28.894'	56°52.269'	x		
So17-45	Gabbro	B	28°28.262'	56°51.895'	x		

TABLE DR2: REPRESENTATIVE ANALYSES OF MINERALS

Mineral	Lawsonite in gabbro	Lawsonite in vein	Plagioclase in pseudotachylite	Fassaitic Cpx in pseudotachylite	Glaucophane in pseudotachylite
Sample	**So15-31-1**	**So15-29**	**pst**	**pst**	**pst**
SiO_2	38.97	38.89	53.73	47.10	56.18
TiO_2	0.00	0.00	0.13	1.94	-
Al_2O_3	31.93	31.82	26.59	7.56	19.71
Cr_2O_3	0.02	0.03	0.04	-	-
FeO	0.17	0.59	1.29	12.24	3.73
MnO	0.00	0.00	0.01	0.20	0.00
MgO	0.12	0.00	1.46	9.29	10.75
CaO	18.27	18.41	12.44	20.80	0.47
Na_2O	0.01	0.02	4.16	0.70	7.17
K_2O	0.01	0.00	0.10	0.02	-
H2O (est.)	-	-	0.00	0.00	2.00
Sum	89.50	89.76	99.96	99.85	98.00
#(O, OH)	8.00	8.00	8.00	6.00	23.00
Si	2.02	2.02	2.45	1.79	7.41
Ti	0.00	0.00	0.00	0.06	-
Al	1.95	1.94	1.43	0.34	3.06
Cr	0.00	0.00	0.00	0.00	-
Fe^{3+}	0.01	0.03	0.00	0.03	0.00
Fe^{2+}	0.00	0.00	0.05	0.36	0.41
Mn	0.00	0.00	0.00	0.01	-
Mg	0.01	0.00	0.10	0.53	2.11
Ca	1.01	1.02	0.61	0.85	0.07
Na	0.00	0.00	0.37	0.05	1.83
K	0.00	0.00	0.01	0.00	-
End-members	-	-	Ab0.38 An0.62	-	-